Lab on a Chip

Dynamic Article Links

Cite this: *Lab Chip*, 2011, **11**, 2509

www.rsc.org/loc

PAPER

Tunable 3D droplet self-assembly for ultra-high-density digital micro-reactor arrays†

Andrew C. Hatch,[a] Jeffrey S. Fisher,[a] Stephen L. Pentoney,[b] David L. Yang[b] and Abraham P. Lee*[a]

Received 2nd November 2010, Accepted 17th May 2011
DOI: 10.1039/c0lc00553c

We present a tunable three-dimensional (3D) self-assembled droplet packing method to achieve high-density micro-reactor arrays for greater imaging efficiency and higher-throughput chemical and biological assays. We demonstrate the capability of this platform's high-density imaging method by performing single molecule quantification using digital polymerase chain reaction, or digital PCR, in multiple self-assembled colloid-like crystal lattice configurations. By controlling chamber height to droplet diameter ratios we predictively control three-dimensional packing configurations with varying degrees of droplet overlap to increase droplet density and imaging sensor area coverage efficiency. Fluorescence imaging of the densely packed 3D reactor arrays, up to three layers high, demonstrates high throughput quantitative analysis of single-molecule reactions. Now a greater number of microreactors can be observed and studied in a single picture frame without the need for confocal imaging, slide scanners, or complicated image processing techniques. Compared to 2D designs, tunable 3D reactor arrays yield up to a threefold increase in density and use 100% of the sensor's imaging area to enable simultaneous imaging a larger number of reactions without sacrificing digital quantification performance. This novel approach provides an important advancement for ultra-high-density reactor arrays.

Introduction

Lab-On-a-Chip micro-wells and droplet-reactors have demonstrated remarkable abilities to perform high throughput chemical and biological assays including: single-cell and single-organism analysis, DNA assays, drug discovery, directed evolution, protein crystallization, chemical synthesis, and single molecule DNA detection.[1–15] Recent publications present particular advantages of droplets and emulsions over standard microwells for high throughput biology applications.[16–22] Among these include the ability to dynamically alter droplet volume and perform automated reaction steps on individual droplet reactors with both pre- and post-processing either on or off chip.

One common limitation associated with droplet based biochemical experiments is a limited reactor number in the imaging field of view while performing simultaneous imaging of multiple droplet reactors. This is particularly relevant for early pathogen detection or quality control screening where biomarkers exist in low concentrations and require the analysis of larger volumes or more reactors.[23] To predictively operate in the digital assay regime of a single-molecule per droplet, Poisson distribution encapsulation efficiencies necessitate a large number of empty droplets relative to positive droplets thus limiting the maximum efficiency of the digital reactor array. Although recent techniques have been developed to overcome Poisson distribution limitations for large particles such as cells and beads,[24–26] these methods do not work for small molecules such as proteins, plasmids, toxins, enzymes, RNA, or short DNA strands. The high throughput demands of these miniaturized array platforms are quickly exceeding the current methods available for imaging throughput both in terms of resolution and field of view.

Although many micro-well and droplet-reactor arrays allow for continuous image capture of a large number of reactions simultaneously,[27–32] to date they have been limited to a single layer, or two-dimensional (2D), array structure. Fabrication limitations, intrinsic patterning schemes and volumetric scaling laws of these 2D arrays result in a loss of as much as 10%–50% of the useable array footprint and prohibit further increases in array density. Using droplet arrays one gains the advantage of droplet self-assembly into close-packed colloidal formations with only thin-film spacing between reactors, thus overcoming

---

[a] *Department of Biomedical Engineering, University of California-Irvine, 3120 Natural Sciences II, Irvine, CA, 92697, USA. E-mail: aplee@uci.edu; Fax: +949-824-1727; Tel: +949-824-9691*

[b] *Beckman Coulter, Inc., 250 S. Kraemer Blvd., Brea, CA, 92821, USA. E-mail: dlyang@beckman.com; Fax: +714-961-3971; Tel: +714-961-3112*

† Electronic supplementary information (ESI) available: in ESI 1, Videos demonstrate droplet self-assembly as a function of droplet chamber height and images demonstrate large field-of-view brightfield and fluorescence images of droplets in high-density arrays. ESI 2 details the calculations used to determine packing properties summarized in table 1. ESI 3 details image processing techniques used for digital PCR quantification. See DOI: 10.1039/c0lc00553c

many of the fabrication limitations associated with high-density array patterning.

Unfortunately, their spherical shapes still impose less than optimal circle packing like arrangements when limited to a single-layer 2D array pattern. These adverse scaling effects and shape factorsmake it difficult to further extend the density of 2D reactor array designs beyond the physical volume restrictions and chemical limitations imposed by the reactions they are meant to contain. Currently these losses are compensated for by using automated high throughput scanning devices such as slide scanners, plate readers, or translational stage microscopes, but these are serial in nature and do not allow rapid monitoring of all reactors simultaneously.

By observation, most biological and chemical droplet based reactions contain transparent fluid materials that allow for visualization of underlying objects and features. We exploit this optical behavior by predictively patterning multilayer droplet arrays with tunable levels of overlap and area coverage then image through each droplet plane to form high density arrays for bio-chemical assays. Previous works demonstrate the use of geometric restrictions in microfluidic channels, and controlling volume ratios of two phase emulsions to drive predictable, close-packed, 3D colloidal structures in microfluidic devices.[33–42] We build upon these techniques and present a unique approach of utilizing tunable 3D droplet arrays to perform fluorescence imaging of biological and chemical reactions in a greater density and utilize camera sensor pixels more efficiently.

This work performs an empirical and mathematical study of various droplet array patterns to describe the tunable degrees of droplet overlap, A_o, and resulting fluorescence transmission intensities of their image projections. This method achieves higher density arrays by reducing the need to further modify a reactor's volume, size, or shape to pack them closer together. Its practicality and usefulness for high-throughput digital-biology applications is demonstrated by performing digital Polymerase Chain Reaction (dPCR) experiments in five different crystalline lattice configurations. Higher density droplet array visualization can now be achieved in tunable degrees with as much as a threefold increase in reactor density and 100% usage of the array area compared to 2D or single plane droplet array patterns.

Theory

3D crystal lattice droplet packing model

Performing a three-dimensional study of colloidal droplet self-assembly in multilayer colloidal crystal like patterns provides a predictive model for determining resultant patterns and image projections of the high-density monodisperse droplet arrays. The interfacial tension between immiscible phases in the emulsion favors a spherical droplet shape, making a close packed sphere packing model the closest simple approximation for describing colloidal droplet self-assembly. By varying only the vertical dimension of a microfluidic chamber, H, relative to the diameter, D, of a given monodisperse droplet emulsion, a variety of predictive single, double, or triple layer close-packed crystal lattice patterns are achieved. References to the ratio of chamber height H, to droplet diameter D, will hereafter be referred to as H/D.

Common close-packed lattice structures that can be achieved are most easily described using Miller index notation to describe crystallographic planes: namely (111), (110), and (100) lattice like orientations, including three layer hexagonal close packing (HCP) and cubic close packing (CCP) orientations. Other arbitrary lattice patterns are possible, but they are not given specific consideration here. Fig. 1 illustrates predictable close-packed colloidal crystal patterns expected for monodisperse droplet emulsions in five different H/D configurations. Tuning H/D to different values creates patterns ranging from single layer hexagonal droplet configurations to multilayer droplet configurations with tunable degrees of overlap and droplet density. For n multiple layers in (111) like lattice structures, the vertical pitch, ΔH, between droplet layers becomes $\sqrt{2/3} \times D$, and for (100) structures the vertical pitch becomes $\sqrt{2}/2 \times D$.

The droplet density, ρ_A, of the various lattice configurations can be calculated using eqn (1) defined as the inverse of a single droplets unit area A_u as follows:

$$\rho_A = \frac{1}{A_u} = \frac{1}{D \times D_x} \tag{1}$$

where A_u is the square area of the chamber which contains exactly 1 droplet. This area is determined by considering the droplet array as repeating rows of droplets with a center to center spacing of one droplet diameter, D, along the row and an effective row spacing, D_x between rows. For H/D ratios from 1 to 1.707, which comprises lattice structures n = 1 (111), and n = 2 (110), and (100); D_x is calculated using eqn (2) derived from its trigonometric relationship with chamber height, H, droplet diameter, D, and droplet radius, r, as follows:

$$\begin{gathered} D_x = \sqrt{D^2 - (H-D)^2 - r^2} \\ \text{where } D \le H \le D\left(1 + \frac{\sqrt{2}}{2}\right) \end{gathered} \tag{2}$$

For *n* additional layers, the effective row spacing becomes D_x/n used to describe the distance which will comprise a single droplet's volume but does not necessarily represent actual row positioning. The optimal water oil, w/o, volume ratio of the droplet emulsion in each array pattern is related to the product of A_u and H as seen in eqn (3) as follows:

$$\text{w/o ratio} = \frac{\frac{4\pi r^3}{3}}{A_u \times H} \tag{3}$$

Table 1 summarizes the interplay between parameters relating to predicted droplet self-assembly for each of the five H/D values. See ESI 1 Video S1 for illustration of theoretical droplet configuration *vs.* H/D between 1–1.707 which demonstrates the transition from single (111) through double (110) to (100) droplet patterns.†

Materials and methods

Microfluidic devices

Microfluidic devices were fabricated from glass and polydimethylsiloxane (PDMS) using standard soft lithography processes.[43] Microfluidic master molds of SU-8 2050 (MicroChem) on 3″ prime silicon wafers were fabricated in a clean-room

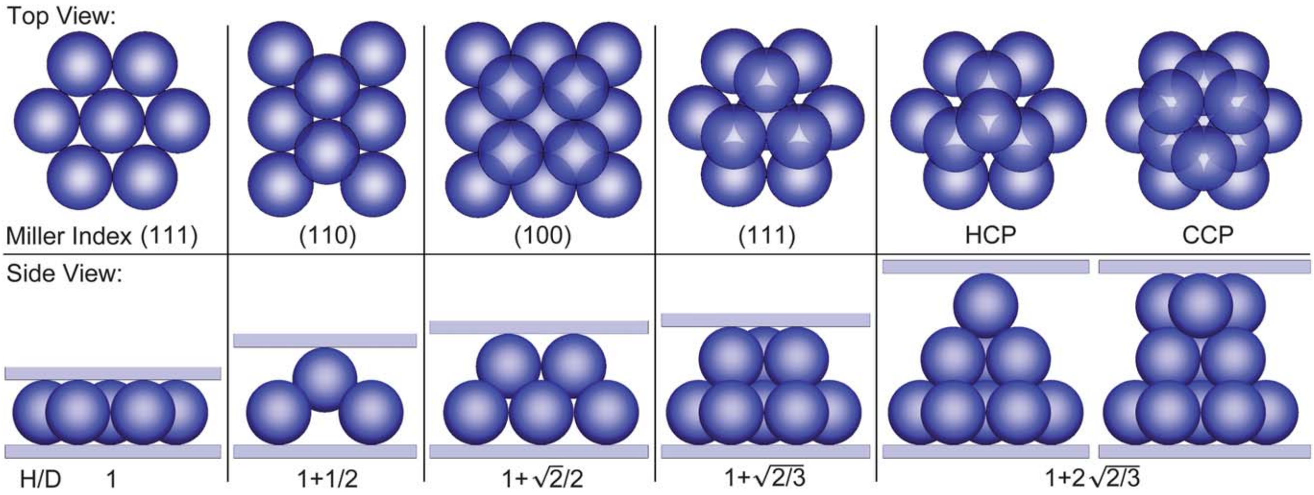

Fig. 1 Three-Dimensional droplet sphere packing configurations Illustration of self-assembled droplet sphere packing configurations as a function of chamber height/droplet diameter ratio (H/D). Top row is a top view of droplets in miller lattice orientations given in order from left to right of single layer (111), double layer (110), double layer (100), double layer (111), and triple layer (111) like HCP and CCP configurations respectively. Bottom row is a side view of the same configurations above, portraying the expected H/D values required to accomplish each cubic lattice droplet pattern using a spherical droplet model. An H/D value of 1 favors single layer (111) like hexagonal packing configurations, H/D of 1.5 favors (110) droplet packing configurations, H/D of 1.707 favors square packed (100) double layer configurations, H/D of 1.816 favors a double layer (111) like hexagonal packing configuration, and finally an H/D of 2.633 yields three layer (111) like hexagonal droplet formations in two possible lattice configurations. These include Hexagonal Close Packing (HCP) shown second to last with top and bottom rows completely overlapping, and Cubic Close Packing (CCP) shown last with all three layers complementarily aligned.

facility using the mask design shown in Fig. 2 and their thicknesses measured using a Dektak profilometer (Veeco). Each device consists of a single SU-8 height designed with oil and PCR inlets, a flow focusing droplet generator, 128 droplet splitter, droplet packing chamber and a single outlet. Sylgard-184 PDMS (Dow Corning) was molded on top of the SU-8 molds following standard curing protocol. The microfluidic devices were assembled by bonding 1mm thick borosilicate 1″ × 3″ glass slides to both the top and bottom of the PDMS molds using air plasma treatment. Due to difficulty of controlling the uniform height of the PDMS molds during the curing stage, bonding them between two glass slides may have slightly compressed or expanded the internal chambers of the microfluidic devices, making the original chamber height measurements only close approximations to the finished device. Some devices showing severe non-uniformity in chamber heights made it difficult to determine the exact H/D

Table 1 H/D driven droplet lattice properties[c]

H/D	1	1 + 1/2 (1.5)	$1+\sqrt{2}/2$ (1.707)	$1+\sqrt{2/3}$ (1.816)	$1+2\sqrt{2/3}$ (2.633)	
Effective Row Spacing (D_x)	$\sqrt{3}\cdot r$	$\sqrt{2}\cdot r$	r	$\sqrt{3}/2\cdot r$	$\sqrt{3}/3\cdot r$	
Number of Droplet Planes (n)	1	2	2	2	3	
Miller index analogue	(111)	(110)	(100)	(111)	HCP[a]	CCP
Sensor Area Coverage Efficiency (%) (A_e)	90.07	98.26	100	97.56	97.56	100.00
Sensor Area Overlap (%) (A_{os})	0	12.81	57.08	83.82	90.69, 83.82[b]	92.69, 79.38[b]
Droplet Area Overlap (%) (A_o)	0	23.07	72.67	92.42	100, 92.42[a]	97.31
Droplet Volume Overlap (%) (V_o)	0	14.27	62.40	90.99	100, 90.99[a]	96
W/O Volume Ratio (%) (w/o)	60.46	49.37	61.24	66.57	68.89	
Droplet Density (drops/mm²) (ρ_A)	546	668	945	1,091	1,637	

[a] For three layer HCP configurations, droplet area and volume overlap calculations have two separate values; the first is for aligned top and bottom layers, the second is for the middle layer. [b] For three layer droplet patterns, two sensor area overlap calculations are given, first corresponds to total overlap, second corresponds to triple overlap. [c] This table summarizes the interplay between parameters relating to predicted colloidal droplet self-assembly in crystal lattice like orientations resulting from five different H/D values. The first row represents the H/D value prediction for common lattice configurations. Row 2 describes the effective row spacing, D_x, between droplet rows in each lattice structure. Row 3 lists the number of droplet planes, n, in each H/D configuration. Miller Index orientations describe the resulting colloidal self-assembled droplet pattern for each H/D value. Sensor area coverage efficiency describes what percentage of the imaging plane is utilized by the droplet lattice structure and sensor area overlap describes how much of the total imaging area corresponds to overlapping droplet regions. Droplet area overlap describes what percentage of a droplets total area is overlapping with neighboring droplets while droplet volume overlap describes what percentage of that area corresponds to the droplet's total volume. Water/oil (w/o) volume ratios describe the theoretical percentage of discrete aqueous phase *vs.* continuous oil phase in the colloidal spherical droplet lattice structure. Finally, the expected droplet density achievable using 46 μm (50 pL) droplets is calculated for each H/D value.

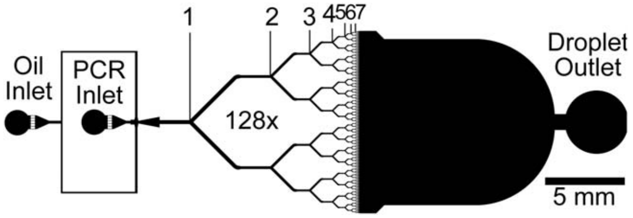

Fig. 2 Microfluidic design of 128 droplet splitter device and droplet-packing chamber. The 128-droplet splitter consists of a 240 μm parent channel that bifurcates 7 times at 45° angles to form 2^7 daughter channels with 30 μm widths. After each bifurcation junction 1–6, the channel width is reduced at a rate of $\sqrt{2}$.

values for their resulting lattice formation in some images and were avoided where possible.

Oil and PCR solutions

This work utilized an oil and surfactant combination that favored high w/o volume ratio emulsions, limited droplet fusion during heating and cooling processes, and reaction compatibility with the Taq-polymerase and other PCR reagents. PCR solutions were prepared using a standard protocol of Amplitaq Gold Fast PCR Master Mix, UP (2X) PCR kit (Applied Biosystems) and custom Taqman forward/reverse primer pairs, DNA strands, and fluorescent Taqman probes (Advanced Biotechnologies Inc.). Solutions were prepared as 20 μL reactions with the following final concentrations: forward/reverse primers (0.9 μM), probe (0.3 μM), 1x PCR master mix, and approximately 3,000 DNA copies. BSA (3–5 μg μL^{-1}) was added to the solution to reduce surface adsorption of DNA or enzymes to the PDMS substrate or tubing, and helped further stabilize the droplet emulsions. The oil phase was prepared from heavy mineral oil with 2–3% wt./wt. EM90 and 0.05% wt./wt. Triton-X 100 as stabilizing surfactants.

Droplet emulsion generation

PCR and oil solutions were loaded into Tygon microbore tubing then injected into microfluidic devices using Pico-Plus syringe pumps (Harvard Apparatus). A flow focusing droplet generator formed the initial droplet emulsion then seven subsequent bifurcation junctions further split the primary droplet into 128 smaller droplets. Droplet generation was performed at flow rates of 4 μL $\min^{-1}$ PCR solution and 2 μL $\min^{-1}$ oil resulting in total droplet generation frequencies of 1.33 kHz and a 66% w/o volume ratio. Other volume ratios were generated by adjusting the w/o flow rate ratio then adjusting the combined flow rates to create a shear profile favoring droplet sizes with the desired 50 pL volume. After droplets finished forming and splitting, they entered a 1 cm × 1.2 cm chamber area with vertical heights varying from 40 to 130 μm. After the droplets filled the chamber, all inlets and outlets were clamped shut to prevent fluid flow in or out of the chamber.

Sphere-packing modeling

Common crystal lattice orientations of (111), (100), (110) and HCP configurations were drawn in Solidworks 2009 software to replicate three-dimensional geometric close-packed droplet configurations. The resulting 3D volume properties and 2D area coverage properties were calculated using Solidworks 2D and 3D analysis tools. These results were validated using Matlab code to generate 2D mappings of circle overlap structures and trigonometric and geometric identities to calculate volume ratios, area ratios, and overlapping calculations See ESI 2 for detailed processing.† This information was used as the basis to design tunable multilayer droplet arrays for higher density packing.

Thermocycling apparatus

Microfluidic devices were thermo-cycled on a Thermo Electric Cooler (TEC) controlled using the company supplied FTC-100 controller hardware and software (Ferrotec Inc). Temperature feedback to control the thermocycling apparatus was accomplished by inserting a thin copper plate with an embedded thermocouple between the microfluidic and TEC device. A custom-fabricated liquid-cooled aluminum block was placed beneath the TEC device to dissipate waste heat. Two-step PCR thermocycling was initiated with a 10 min hot start at 95 °C to activate the enzymes. Following this, 40 temperature cycles, alternating between 58 °C and 95 °C with a 20 s hold at each of these temperatures, allowed amplification of the nucleic acid. Temperature ramp rates of 2–3 °C s^{-1} were used for both heating and cooling.

Digital quantification

Fluorescence images were captured on an inverted fluorescence microscope (Olympus) with a monochrome cooled CCD camera (Hamamatsu) and images captured using Wasabi (1.4.2) capture software. ImageJ[44] software was used to detect and quantify fluorescent droplets and analyze their size, shape, color, fluorescence intensity, spacing, radial profile, droplet patterns, edge detection schemes, and watershed separation schemes. Background subtractions, contrast enhancement, and flatfield corrections were performed as needed during quantification of results (see ESI 3 for more details †). These results were then compared to the expected number of positive droplets predicted from Poisson statistics for serial dilutions of the known sample concentration.

Results and discussion

3D droplet self-assembly

With a predictive model in place, monodisperse droplet emulsions were generated in microfluidic devices and H/D values varied to analyze the resulting self-assembled droplet packing conformations. Dynamic H/D control was achieved by adjusting droplet diameter for a given chamber height, or changing the height of the chamber while using a given droplet size. Fig. 3 presents images of droplet configurations in common Miller index configurations achieved using the same five H/D values previously mentioned. See ESI 1 Video S2, Video S3 & Video S4 which show the rapid self-assembly of droplets in (110), (100), and (111) droplet like formations as they enter or flow through thin height microfluidic chambers. ESI 1 Fig. S1 & Fig. S2 show larger field of view images of droplets in double layer (111) and

(100) formations respectively.† In these images it is seen that grain boundaries and lattice impurities may occur as commonly seen in colloidal lattice structures.

In the three-layer droplet packing configurations, both hexagonal close-packed (HCP) and cubic close-packed (CCP) configurations were expected to occur with equal probability based on the assumption that there is a negligible difference in energy states between their conformations. However, no CCP configurations were observed in the experiments performed, indicating that due to initial conditions, there may be an energy barrier to overcome when dynamically organizing into CCP lattice orientations. For this reason they are not presented in this work. Possible solutions to overcome this problem may involve using higher H/Ds and lower w/o ratios to relax the droplet density and allow more shifting of the droplet planes. Another solution may be to use a sudden expansion and reduction of the chamber height to drive a sudden relaxation, shift, and gradual recompression of the droplet emulsion, inducing a switch from an HCP to a CCP orientation.

Image processing analyses of droplet lattice orientations as a function of H/D value and water to oil (w/o) ratio showed that droplets assembled into (111), (110) and (100) cubic lattice like orientations with less than 5% standard deviation in droplet density from expected values ($N = 10{,}000$ per orientation). This error accounts for variations arising from droplet lattice defects, droplet monodispersity, and slight droplet deformations occurring in the close-packed droplet arrays. The use of w/o ratios not corresponding to model predictions based on spherical droplet shapes resulted in either deformed droplets packed closer together, or loosely packed droplets with disordered patterns, similar to work presented by Shui *et al.*[33] Based on our experimental results, a 46 μm (50 pL) droplet size would be expected to achieve double and triple layer (111) pattern densities of 1,092 ± 55 (s.d.) to 1,638 ± 81 (s.d.) droplets/mm^2 respectively. These high reactor densities of $n = 2$ or 3 layers provide up to threefold increases in droplet density, ρ_A, compared to $n = 1$ patterns or the highest density microreactors published to date.[27]

One major advantage of the colloidal self-assembly of 3D droplet reactors in a tunable multi-planar array is the dramatic increase in density for visualizationor greater area coverage and economy of scale without sacrificing droplet volume. Although droplet deformations in close-packed arrays make it difficult to fully predict the exact packing density and droplet morphology, it offers some advantages as well. Self-assembly of rigid spherical particles in confined regions will often pack more loosely because they cannot easily slide past one another. Droplets on the other hand, will readily shift and deform to fill in vacancies and better adapt to confined geometries. The amount of deformation a droplet will exhibit is dependent on the w/o volume ratio, the confined geometry, and the interfacial tension between the two liquids as described by Kottke *et al.*[34] This behavior may very well explain why triple layer H/D configurations favor HCP patterns over CCP patterns.

Droplet stability

On chip droplet stability testing of close packed arrays, and subsequent digital PCR studies, were performed to demonstrate the potential of higher-density droplet arrays for digital biology applications. With close packed droplet formations and high w/o volume ratios, droplets have a tendency to coalesce together. By using an appropriate combination of oil and water phase stabilizing surfactants, the droplet reactor arrays withstood PCR temperatures between 58–95 °C for over 40 amplification cycles with droplet coalescence of less than 0.1% ($N = 100{,}000$).

One difficulty with emulsion stability observed when using polydimethylsiloxane (PDMS) devices, is that the continuous phase mineral oil can vaporize and escape through the PDMS material. This effect is much more problematic if heated for prolonged periods as previously published by Courtois *et al.*[1,45] Embedding a thin glass coverslip directly covering the chamber in the PDMS material dramatically reduced this behavior. It also served to reduce physical deformations of the chamber walls caused by pressure driven flow and/or thermal expansion. Another complicating factor when performing PCR on microfluidic devices is the presence of small air bubbles trapped in the device. These air bubbles dynamically expand and contract during thermocycling causing extreme fluctuations in pressure; experiments where this occurred were excluded from our experimental analysis. This occurrence was dramatically reduced by first pre-filling the entire device with oil before performing droplet generation and droplet emulsion filling of the device.

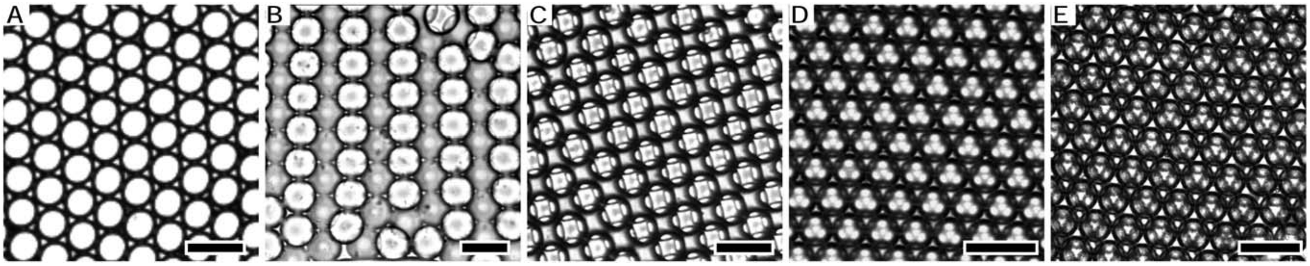

Fig. 3 Brightfield images of single layer to triple layer self-assembled droplet sphere packing configurations. Scale bars are 100 μm. **(A)** single layer hexagonal droplet-packing in (111) configuration with a 46 μm tall channel and 48 μm diameter droplets. **(B)** double layer (110) like packing of 63 μm droplets in an 82 μm tall chamber. Note the H/D here is only1.3, indicating a slightly more disperse packing formation than a true (110) formation. **(C)** double layer square packing in (100) configuration with 46 μm droplets in a chamber height of 78 μm. **(D)** double layer hexagonal (111) packing with 44 μm droplets in an 80 μm tall chamber. **(E)** triple layer (111) like HCP configuration of 52 μm diameter droplets in a 130 μm tall chamber. Note the droplet height required for triple hexagonal packing is slightly lower than the 136 μm height prediction due to the deformability of the droplets and slight deformation of PDMS chamber height making it difficult to determine the exact H/D value.

Selecting the appropriate oil phase and stabilizing surfactants for reaction compatibility and droplet stability is important for their function as an inert and stable volume-reactor. As most DNA based reagents and enzymes have a highly polarized structure, they have a strong propensity to remain in the aqueous phase in the emulsion. However, some proteins and molecules may migrate to or through the oil/water interface depending on their size and amphiphilic properties.[45] Alternative surfactant/oil combinations such as perfluorinated polyethers- polyethyleneglycol block-copolymer surfactant (PFPE-PEG) in fluorinated oils may be utilized to minimize this effect.[46,47] Still, The compounds of primary interest in these experiments, target DNA strands and fluorophores, were not observed to readily transmit across, or get absorbed into, the droplet-droplet interfaces. This is evident in the experimental results by the large number of individual fluorescent droplets surrounded by non-fluorescing droplets as seen in Fig. 4, and the high level of correspondence between predicted and experimental digital PCR results. See ESI 1 Fig. S3 for a large field-of-view (3.5 mm^2) fluorescence image of droplets in double layer (111) packing which further demonstrates low droplet coalescence during thermocycling and performance for fluorescence imaging.†

Digital PCR quantification

Droplet based digital PCR experimental results were determined from end-point fluorescence microscopy images of 1 cm^2 areas containing 100,000 droplets or more. In addition to the PCR experiments performed for each packing configuration shown in Fig. 4, completion of three independent droplet PCR experiments in double layer (111) packing configurations were performed to demonstrate the capability of multilayer, $n > 1$, digital PCR imaging and analysis for quantitative digital biology applications. The samples contained DNA concentrations of 3,000 copies per 20-μL reaction volume and discretized into 50 pL droplets yielding a Poisson distribution prediction of one positive droplet in 133 ± 11.5 (s.d.) negative droplets. The experiments yielded on average one positive droplet in 131 ± 5 (s.d.) negative droplets ($N = 100,000$) per experiment. This close correspondence between experimental and predicted results demonstrates repeatable precision and performance of this high-density design to resolve and detect digital biology reactions in multilayer droplet images. The close correlation between end-point fluorescence images and the number of positive fluorescing droplets with the sample's starting DNA template concentration indicates low loss of sample to surrounding oil media or microfluidic devices. In addition, accurate digital quantification is achieved because Poisson probability distributions predict a low probability of encapsulating more than a single DNA copy per droplet, less than 5% error, when assuming random DNA encapsulation frequencies of less than 5% of the total number of droplet reactors‡.

Fluorescence intensity imaging analysis

Fluorescence images were further analyzed to determine the relative variation in excitation and emission intensities for droplets in $n = 1,2$, or 3 planes. Droplet fluorescence levels vary as a function of n because of light absorption, reflection, and scattering at each successive droplet oil interface. Fig. 5 contains radial profile plots and surface intensity plots of droplets in each layer of the varying droplet pattern formations demonstrating the level of fluctuation exhibited in each droplet's fluorescence intensity. Fig. 5C demonstrates that for $n = 1$ or 2 fluorescence excitation profiles, maximum intensity is relatively unchanged near the center of the droplet where there is no overlap but, a reduction occurs in the immediate vicinity of overlapping edges with other droplets. In the remaining regions of the overlapping droplet areas, fluorescence emission still transmits through with less than 5% attenuation. Droplets residing on the third layer in an $n = 3$ HCP formation suffer from more severe interference from droplets in the uppermost layer resulting in as much as 40% attenuation in image interensity. This dramatic reduction indicates that the scattering of light, focal depth, and light transmission play crucial roles as n increases.

Droplet array overlap

Upon inspection, it is apparent that the non-overlapping droplet areas in the imaged array also correspond to the thickest central droplet regions containing the majority of fluorescence signal information. More than 65% of the volume of a sphere is located within the central 50% of the droplet's imaged area. Based on the calculations in Table 1 which compare overlap percentages of both area and volume, some configurations yield as much as 10% lower volume overlap than area overlap, indicating a favorable economy in information for those designs. In the (100) square packing image shown in Fig. 5B, the total area coverage increases to 100% of the imaging plane with more than 35% of the total droplet volume residing in the non-overlapping central droplet regions. Two mechanisms are possible for determining each overlapping droplets average intensity, 1. Exclusive use of a droplets central region, or 2. Utilize the entire droplet area by interpolating each droplets contribution to the overlapping areas. This is achievable because as seen in Fig. 4 C & D, fluorescence intensities of two overlapping fluorescent droplets have brighter fluorescence levels in those regions, demonstrating an additive contribution to fluorescence intensity. As seen in Fig. 5A, the overlapping droplet regions can still transmit as much as 90% of their original intensity. The Use of automated image processing algorithms to perform pattern recognition, image correction, and quickly analyze complex patterns, may further increase the high-throughput potential of this design by allowing lower magnification imaging for higher fields of view.

Assays with extremely high concentrations of positive droplets that express non-uniform fluorescence intensities, such as cell expression assays in super-Poisson encapsulation efficiencies, fluorescence analysis of higher order 3D arrays may suffer from greater background levels and droplet-droplet cross-talk. As this would make fluorescence imaging and quantification more difficult, lower order patterning in (110) or (100) configurations would be more suitable and could be selected by controlling H/D ratios to suit the assay. Although the increase in density is less dramatic, the gain in sensor area coverage would be useful. Assays with low concentrations of positive droplets that express uniform fluorescence levels, such as low concentration

---

‡ Poisson Statistics for digital PCR based on a probability distribution that $P(k = 1)$ and setting error $P(k = 1)/\lambda \leq 0.05$ and solving for λ.

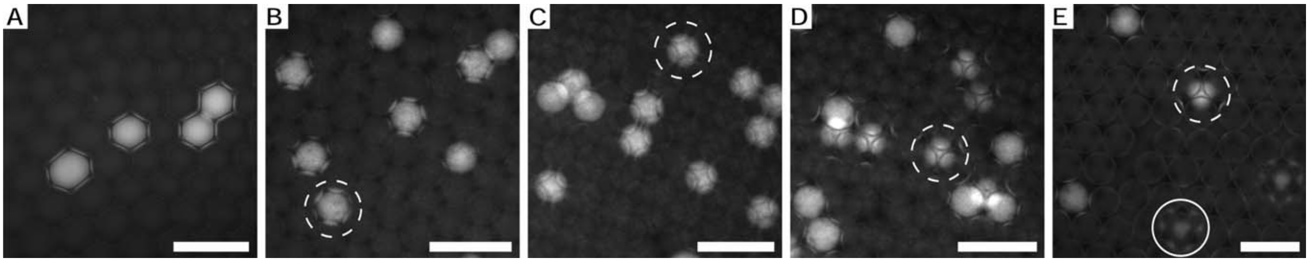

Fig. 4 Fluorescence images of digital PCR amplified droplets in single to triple layer self-assembled sphere packing configurations. Scale bars are 100 μm. **(A)** single layer (111) droplet stacking. **(B)** double layer (110) packing. **(C)** double layer (100) square packing. **(D)** double layer (111) packing. **(E)** triple layer HCP packing. Dashed circles represent droplets in second layer while solid circle represents droplets in third layer.

single-molecule detection, tolerate higher levels of overlap making two and even three layer configurations more suitable.

Due to the low DNA copy number of the sample solutions tested in the three layer (111) HCP designs, the probability of having two positive droplets in overlapping top and bottom layer configurations is low, therefore no images demonstrating this were captured. One would expect that higher target concentrations would increase the probability of this happening. However, previous discussions suggest that even in this scenario, end-point quantification could still distinguish between the brighter fluorescence intensity of two overlapping positive droplets if all droplets express the same relative fluorescence intensity. Better still; a three layer CCP droplet pattern would avoid direct overlapping of the first and third layer making it highly favorable to perform future research to further investigate ways to preferentially achieve this pattern.

Multilayer droplet imaging

One primary benefit of using three-dimensional droplet patterning to increase droplet density is that it requires a smaller area to both visualize and fluorescently excite the same number of reactors. The smaller field of view allows for a higher imaging magnification if desired, and for the excitation light source to be used more efficiently to increase the overall fluorescence excitation intensity. This occurs because the marginally diminished light that would have normally transmitted through the first layer and gone unused now passes through to subsequent droplet layers yielding greater usage of fluorescence excitation illumination. Furthermore, by allowing reactor areas to overlap, pixels on the imaging sensor are used more efficiently. This economy in pixel resolution is actually two fold. First, the area coverage of the imaging sensor is increased to 100% meaning all available pixels are used. Second, by allowing image projections of overlapping droplet reactors that are predictably patterned on the imaging sensor, a higher magnification can be achieved allowing a greater pixel/droplet resolution, or allow a lower resolution imaging sensor with some pixels shared among droplets and some not.

Forming similar high density 3D arrays using traditional rigid substrate reactor arrays would require complicated fabrication techniques that so far have been incapable of achieving such close proximity reactor planes that are also easy to fill and handle. A larger spacing between reactor planes would make it difficult to resolve multiple layers of wells using typical microscope objective depths-of-field of 5–100 μm. With our system, droplet spacing from the mid-plane of the first layer to the mid-plane of the third layer is as low as 75 μm for a 46 μm droplet. This close spacing allows the majority of all three layers to be simultaneously resolved in a single snapshot. Alternatively, biasing focus toward the furthest layer to compensate for its more obscured path from the imaging sensor yields a more even

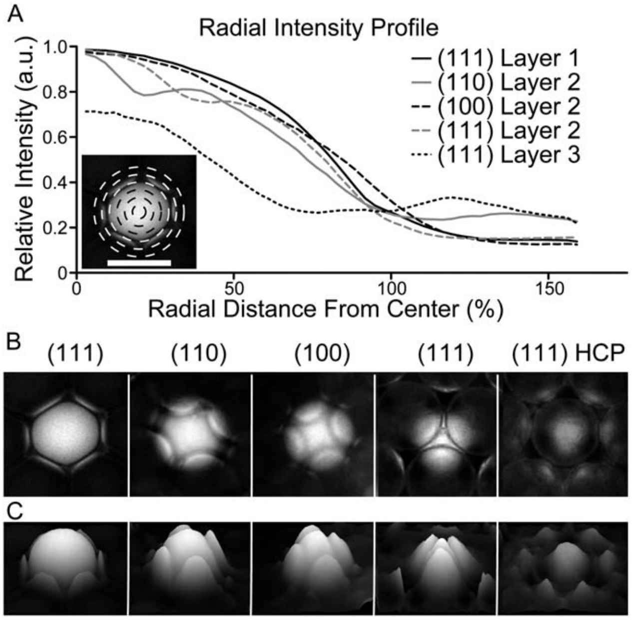

Fig. 5 Analysis of droplet fluorescence intensity as a function of droplet position in the lattice plane is analyzed by comparing radial intensity profiles and fluorescence images of each type observed. **(A)** Radial profile plot of fluorescent droplets measured from center of fluorescent droplet outwards comprising n = 1 (111), n = 2 (110), (100), (111) and n = 3 (111) HCP lattice formations (N ≥ 2). Notice the average decrease in relative intensity between n = 1 and n = 2 is less than 10–20%, whereas the third layer in n = 3 is reduced by as much as 50%. (Inset is an illustration of droplet image with concentric rings defining 25% radial distance intervals from which averaged intensity profile measurements are taken). Scale bar is 50 μm. **(B)** Composition of enlarged single droplet images in each lattice structure position with relative intensity adjustment and contrast enhancement performed to emphasize intensity profiles over the imaging plane. **(C)** three-dimensional intensity surface plots of the same images in **(B)** for better profile visualization. Left to right, fluorescence intensity images are n = 1 (111), second layer of n = 2 (110), (100), and (111), and third layer of n = 3 HCP droplet positions. Fluorescent images in **(B)** and **(C)** are compiled from separate images with intensity profiles normalized to the top droplet layers fluorescence intensity.

representation of all three layers. Backside illumination for fluorescence excitation can also help compensate for the bottom layers obscured path by increasing its fluorescence excitation relative to those above.

Refractive index (RI) matching, both of the microfluidic substrate material as well as the fluid emulsion, can play considerable roles in the overall imaging performance of high-density droplet emulsions. In particular, RI mismatch of the fluid phases forming the droplet emulsion would be expected to cause localized lensing and scattering effects which adversely influence light transmission and clarity.[48] Because of this behavior, RI optimization of the microfluidic devices and fluid phases could yield improved performance of multilayer droplet packing arrays by improving signal to noise ratios. It would be expected that the imaging quality for these devices will vary depending on the overall droplet size (radius of curvature will affect lensing properties), pattern formation in the array, refractive index matching of the solutions, and the direction of illumination for fluorescence excitation. RI mismatches between the continuous and discrete phases can be modified using additives in the aqueous phase, *e.g.* glycerol, Ficoll, or sucrose, or selecting different oils like fluorocarbon, silicon, and hydrocarbon based oils.

Conclusions

This simple, easy to implement approach of controlling chamber height to tune droplet emulsion patterns within microfluidic devices enables optimal imaging of high-density droplet reactor arrays for digital biology and chemistry applications. Discretizing reaction samples into highly monodisperse droplet emulsions enables single molecule or single cell assays to occur independent of the bulk phase or population in which they normally reside, and yields quantifiable and statistically relevant results. Depending on a particular assay's imaging tolerance for droplet overlap, reactor density can be considerably increased using close-packed multi-layer droplet formations. High-density packing reduces the need to modify a reactors' size, shape, or volume, which could otherwise yield adverse consequences in usability, fabrication complexity, or reaction compatibility. This versatile self-assembled 3D colloidal crystalline patterning of droplets into optimized high-density image projections of droplet arrays is well adapted for imaging on existing commercial instruments and provides a fundamental basis for future research.

Acknowledgements

This work was supported in part by the Defense Advanced Research Projects Agency (DARPA) N/MEMS S&T Fundamentals program under grant no. HR001-06-1-0500 issued to the Micro/nano Fluidics Fundamentals Focus (MF3) Center. Authors also thank Beckman Coulter Inc. for providing critical reagents relating to the project.

Notes and references

1 F. Courtois, L. F. Olguin, G. Whyte, D. Bratton, W. T. S. Huck, C. Abell and F. Hollfelder, *ChemBioChem*, 2008, **9**, 439–446.

2 B. T. Kelly, J. Baret, V. Taly and A. D. Griffiths, *Chem. Commun.*, 2007, 1773–1788.

3 Y. Schaerli and F. Hollfelder, *Mol. BioSyst.*, 2009, **5**, 1392–1404.

4 V. Taly, B. T. Kelly and A. D. Griffiths, *ChemBioChem*, 2007, **8**, 263–272.

5 J. Baret, V. Taly, M. Ryckelynck, C. A. Merten and A. D. Griffiths, *médecine/sciences*, 2009, **25**, 627–632.

6 J. J. Agresti, E. Antipov, A. R. Abate, K. Ahn, A. C. Rowat, J. Baret, M. Marquez, A. M. Klibanov, A. D. Griffiths and D. A. Weitz, *Proc. Natl. Acad. Sci. U. S. A.*, 2010, **107**, 4004–4009.

7 J. R. Rettig and A. Folch, *Anal. Chem.*, 2005, **77**, 5628–5634.

8 N. R. Beer, B. J. Hindson, E. K. Wheeler, S. B. Hall, K. A. Rose, I. M. Kennedy and B. W. Colston, *Anal. Chem.*, 2007, **79**, 8471–8475.

9 N. R. Beer, E. K. Wheeler, L. Lee-Houghton, N. Watkins, S. Nasarabadi, N. Hebert, P. Leung, D. W. Arnold, C. G. Bailey and B. W. Colston, *Anal. Chem.*, 2008, **80**, 1854–1858.

10 Y. Zhang and P. Ozdemir, *Anal. Chim. Acta*, 2009, **638**, 115–125.

11 R. A. White, P. C. Blainey, H. C. Fan and S. R. Quake, *BMC Genomics*, 2009, **10**, 116.

12 T. Xu, P. Thwar, V. Srinivasan, V. K. Pamula, and K. Chakrabarty, in *2007 IEEE/NIH Life Science Systems and Applications Workshop, LISA*, Institute of Electrical and Electronics Engineers Computer Society, Piscataway, NJ 08855-1331, United States, Bethesda, MD, United States, 2007, pp. 140–143.

13 Y. Zeng, R. Novak, J. Shuga, M. T. Smith and R. A. Mathies, *Anal. Chem.*, 2010, **82**, 3183–3190.

14 Z. Hua, J. L. Rouse, A. E. Eckhardt, V. Srinivasan, V. K. Pamula, W. A. Schell, J. L. Benton, T. G. Mitchell and M. G. Pollack, *Anal. Chem.*, 2010, **82**, 2310–2316.

15 E. Brouzes, M. Medkova, N. Savenelli, D. Marran, M. Twardowski, J. B. Hutchison, J. M. Rothberg, D. R. Link, N. Perrimon and M. L. Samuels, *Proc. Natl. Acad. Sci. U. S. A.*, 2009, **106**, 14195–14200.

16 P. Garstecki, H. A. Stone and G. M. Whitesides, *Phys. Rev. Lett.*, 2005, **94**, 164501.

17 S. Y. Teh, R. Lin, L. H. Hung and A. P. Lee, *Lab Chip*, 2008, **8**, 198–220.

18 A. Huebner, S. Sharma, M. Srisa-Art, F. Hollfelder, J. B. Edel and A. J. deMello, *Lab Chip*, 2008, **8**, 1244–1254.

19 A. D. Griffiths and D. S. Tawfik, *Trends Biotechnol.*, 2006, **24**, 395–402.

20 H. M. O'Hare and K. Johnsson, *Chem. Biol.*, 2005, **12**, 1255–1257.

21 M. Margulies, M. Egholm, W. E. Altman, S. Attiya, J. S. Bader, L. A. Bemben, J. Berka, M. S. Braverman, Y. Chen, Z. Chen, S. B. Dewell, L. Du, J. M. Fierro, X. V. Gomes, B. C. Godwin, W. He, S. Helgesen, C. H. Ho, G. P. Irzyk, S. C. Jando, M. L. I. Alenquer, T. P. Jarvie, K. B. Jirage, J. Kim, J. R. Knight, J. R. Lanza, J. H. Leamon, S. M. Lefkowitz, M. Lei, J. Li, K. L. Lohman, H. Lu, V. B. Makhijani, K. E. McDade, M. P. McKenna, E. W. Myers, E. Nickerson, J. R. Nobile, R. Plant, B. P. Puc, M. T. Ronan, G. T. Roth, G. J. Sarkis, J. F. Simons, J. W. Simpson, M. Srinivasan, K. R. Tartaro, A. Tomasz, K. A. Vogt, G. A. Volkmer, S. H. Wang, Y. Wang, M. P. Weiner, P. Yu, R. F. Begley and J. M. Rothberg, *Nature*, 2005, **437**, 376–380.

22 M. Chabert, K. D. Dorfman, P. de Cremoux, J. Roeraade and J. Viovy, *Anal. Chem.*, 2006, **78**, 7722–7728.

23 K. E. Petersen, W. A. McMillan, G. T. A. Kovacs, M. A. Northrup, L. A. Christel and F. Pourahmadi, *Biomed. Microdevices*, 1998, **1**, 71–79.

24 A. R. Abate, C. Chen, J. J. Agresti and D. A. Weitz, *Lab Chip*, 2009, **9**, 2628–2631.

25 J. F. Edd, D. Di Carlo, K. J. Humphry, S. Koster, D. Irimia, D. A. Weitz and M. Toner, *Lab Chip*, 2008, **8**, 1262–1264.

26 M. Chabert and J. Viovy, *Proc. Natl. Acad. Sci. U. S. A.*, 2008, **105**, 3191–3196.

27 P. Pantano and D. R. Walt, *Chem. Mater.*, 1996, **8**, 2832–2835.

28 E. A. Ottesen, J. W. Hong, S. R. Quake and J. R. Leadbetter, *Science*, 2006, **314**, 1464–1467.

29 D. A. Wheeler, M. Srinivasan, M. Egholm, Y. Shen, L. Chen, A. McGuire, W. He, Y. Chen, V. Makhijani, G. T. Roth, X. Gomes, K. Tartaro, F. Niazi, C. L. Turcotte, G. P. Irzyk, J. R. Lupski, C. Chinault, X. Song, Y. Liu, Y. Yuan, L. Nazareth, X. Qin, D. M. Muzny, M. Margulies, G. M. Weinstock, R. A. Gibbs and J. M. Rothberg, *Nature*, 2008, **452**, 872–876.

30 C. H. J. Schmitz, A. C. Rowat, S. Koster and D. A. Weitz, *Lab Chip*, 2009, **9**, 44–49.

31 S. O. Sundberg, C. T. Wittwer, C. Gao and B. K. Gale, *Anal. Chem.*, 2010, **82**, 1546–1550.

32 F. Shen, W. Du, J. E. Kreutz, A. Fok and R. F. Ismagilov, *Lab Chip*, 2010, **10**, 2666–2672.

33 L. Shui, E. S. Kooij, D. Wijnperle, A. V. D. Berg and J. C. T. Eijkel, *Soft Matter*, 2009, **5**, 2708–2712.

34 P. A. Kottke, A. Saillard and A. G. Fedorov, *Langmuir*, 2006, **22**, 5630–5635.

35 S. A. Vanapalli, C. R. Iacovella, K. E. Sung, D. Mukhija, J. M. Millunchick, M. A. Burns, S. C. Glotzer and M. J. Solomon, *Langmuir*, 2008, **24**, 3661–3670.

36 Y. Zeng and D. J. Harrison, *Anal. Chem.*, 2007, **79**, 2289–2295.

37 E. Kumacheva, P. Garstecki, H. Wu and G. M. Whitesides, *Phys. Rev. Lett.*, 2003, **91**, 128301.

38 Y. Yin, Y. Lu, B. Gates and Y. Xia, *J. Am. Chem. Soc.*, 2001, **123**, 8718–8729.

39 N. V. Dziomkina and G. J. Vancso, *Soft Matter*, 2005, **1**, 265–279.

40 A. van der Net, G. W. Delaney, W. Drenckhan, D. Weaire and S. Hutzler, *Colloids Surf., A*, 2007, **309**, 117–124.

41 Andrea Fortini and Marjolein Dijkstra, *J. Phys.: Condens. Matter*, 2006, **18**, L371.

42 A. van der Net, A. Gryson, M. Ranft, F. Elias, C. Stubenrauch and W. Drenckhan, *Colloids Surf., A*, 2009, **346**, 5–10.

43 Y. Xia and G. M. Whitesides, *Annu. Rev. Mater. Sci.*, 1998, **28**, 153–184.

44 W. S. Rasband, *ImageJ*, National Institutes of Health, Bethesda, MD, United States, 1997.

45 F. Courtois, L. F. Olguin, G. Whyte, A. B. Theberge, W. T. S. Huck, F. Hollfelder and C. Abell, *Anal. Chem.*, 2009, **81**, 3008–3016.

46 C. Holtze, A. C. Rowat, J. J. Agresti, J. B. Hutchison, F. E. Angile, C. H. J. Schmitz, S. Koster, H. Duan, K. J. Humphry, R. A. Scanga, J. S. Johnson, D. Pisignano and D. A. Weitz, *Lab Chip*, 2008, **8**, 1632–1639.

47 L. S. Roach, H. Song and R. F. Ismagilov, *Anal. Chem.*, 2005, **77**, 785–796.

48 W. Chantrapornchai, F. M. Clydesdale and D. J. McClements, *Food Res. Int.*, 2001, **34**, 827–835.